ACS Catalysis

Research Article

pubs.acs.org/acscatalysis

Unraveling the Dynamic Nature of a CuO/CeO_2 Catalyst for CO Oxidation in *Operando*: A Combined Study of XANES (Fluorescence) and DRIFTS

Siyu Yao,[†,▽] Kumudu Mudiyanselage,[†] Wenqian Xu,[†] Aaron C. Johnston-Peck,[∥] Jonathan C. Hanson,[†] Tianpin Wu,[‡] Dario Stacchiola,[†] José A. Rodriguez,[†] Haiyan Zhao,[‡] Kevin A. Beyer,[‡] Karena W. Chapman,[‡] Peter J. Chupas,[‡] Arturo Martínez-Arias,[§] Rui Si,[†] Trudy B. Bolin,[‡] Wenjian Liu,[▽] and Sanjaya D. Senanayake*[,†]

[†]Chemistry Department, Brookhaven National Laboratory, Upton, New York 11973, United States

[‡]X-ray Science Division, Advanced Photon Source, Argonne National Laboratory, Argonne, Illinois 60439, United States

[§]Instituto de Catálisis y Petroleoquímica, Consejo Superior de Investigaciones Científicas (ICP-CSIC), Madrid E-28049, Spain

[▽]Center for Computational Science & Engineering, and PKU Green Chemistry Center, Peking University, Beijing 100871, People's Republic of China

[∥]Center for Functional Nanomaterials, Brookhaven National Laboratory, Upton, New York 11973, United States

Supporting Information

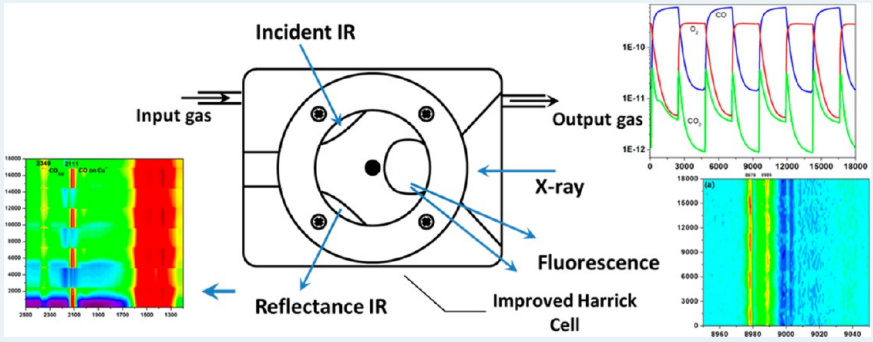

ABSTRACT: The redox chemistry and CO oxidation ($2CO + O_2 \rightarrow 2CO_2$) activity of catalysts generated by the dispersion of CuO on CeO_2 nanorods were investigated using a multitechnique approach. Combined measurements of time-resolved X-ray absorption near-edge spectroscopy (XANES) and diffuse reflectance infrared Fourier transform spectroscopy (DRIFTS) in one setup were made possible with the development of a novel reaction cell in which fluorescence mode detection was applied to collect the XANES spectra. This is the first reported example using XANES in a similar technique combination. With the assistance of parallel time-resolved X-ray diffraction (XRD) measurements under *operando* conditions, we successfully probed the redox behavior of CuO/CeO_2 under CO reduction, constant-flow (steady-state) CO oxidation and during CO/O_2 cycling reactions. A strong copper ↔ ceria synergistic effect was observed in the CuO/CeO_2 catalyst. Surface Cu(I) species were found to exhibit a strong correlation with the catalyst activity for the CO oxidation reaction. By analysis of phase transformations as well as changes in oxidation state during the nonsteady states in the CO/O_2 cycling reaction, we collected information on the relative transformation rates of key species. Elementary steps in the mechanism for the CO oxidation reaction are proposed based on the understandings gained from the XANES/DRIFTS *operando* studies.

KEYWORDS: *Operando catalysis, XANES, DRIFTS, CO oxidation, copper, ceria*

1. INTRODUCTION

Catalysis offers a versatile ability to meet the demands for energy,[1] synthesis of fuels for the future[2,3] and the remediation of environmental pollutants.[4] However, the fundamental understanding of even simple catalytic processes remains difficult, because of the complex nature of processes that occur dynamically between reactants and polycrystalline catalyst materials. The development of *in situ* characterization techniques (scattering, imaging, and other spectroscopy techniques) has made it possible for researchers to identify and monitor reaction intermediates and catalyst structures that evolve under reaction conditions.[5−7] The combination of

Received: February 4, 2014
Revised: April 11, 2014
Published: April 15, 2014

different types of characterization techniques provides an opportunity for a multiangle approach toward understanding the reaction mechanism and the intrinsic nature of the catalyst active phases.[8,9]

Among the currently available experimental setups, the combination of X-ray absorption spectroscopy (XANES) and diffuse reflectance infrared Fourier transform spectroscopy (DRIFTS) techniques is an invaluable pairing of tools that allows one to observe the electronic and structural transitions of catalysts and probe the evolution of low-concentration surface adsorbates simultaneously. Newton and co-workers have made several ground-breaking advances in this field. By coupling energy-dispersive X-ray absorption fine spectroscopy (EDXAFS) and DRIFTS, they managed to study the CO/NO interaction over Rh- and Pd-based catalysts and low-temperature methane oxidation over Pt/Al_2O_3 catalysts with a time scale resolution on the order of seconds.[10−19] The combined DRIFTS and energy scanning transmission technique has been recently developed as an extension of the above techniques.[20,21]

Despite the success of the combination of transmission EDXAFS and DRIFTS, it must be stated that special requirements related to EDXAFS limit the range of its application. EDXAFS and other transmission-based X-ray absorption measurements require an appropriate transmittance to obtain high-quality spectra.[22] The extent of transmittance of the X-ray through a sample is influenced by absorption of the incident X-ray (I_0) as governed by Beer's Law (eq 1):

$$I = I_0 e^{-\mu t} \tag{1}$$

The extent to which the incident X-ray is absorbed is directly proportional to the density (ρ), the thickness (t), and the atomic number (Z) of the sample while being inversely proportional to the atomic mass (A) and the energy of the incident X-ray (E). This relationship is represented by the absorption coefficient (μ) in eq 2:

$$\mu = \frac{\rho Z^4}{AE^3} \tag{2}$$

Incident X-rays will be strongly absorbed (or not transmitted) by materials composed of high-Z atoms and/or if they have low energies.[23] As a result of these factors, it is difficult to obtain transmission measurements involving high-Z metal oxides (e.g., CeO_2, La_2O_3) especially at low energy absorption edges, because this leads to infinite absorbance and zero transmittance. This obstacle is usually avoided by dilution of strongly absorbing material in weakly or nonabsorbing inert media, such as silica or BN. However, heavily diluted materials are difficult to study using transmission, because of a lack of sufficient absorbing material to obtain a detectable absorption. Furthermore, for combined DRIFTS catalytic studies, sample dilution makes identification of the surface adsorbates increasingly difficult, because the concentration of likely active sites has been considerably reduced through dilution, which is a problem that is also manifested in the turnover of reactants and the monitoring of catalyst activity.

X-ray absorption spectroscopy measurements of catalysts also can be performed in the fluorescence mode.[24] Thus, we are motivated in this study to enable a fluorescence mode detection to obtain high-quality spectra without having to dilute samples for *operando* catalytic measurements using combined DRIFTS and XANES. The fluorescence mode measurement is reliant on several complex collective of factors, including the emission of characteristic fluorescence photons (following the core-hole relaxation process), the absorption coefficient (μ), the path length of the emitted photons, the angle of detection, and the ability to minimize self-absorption affects (reabsorption of the emitted photons). This mode is better suited for high-Z elements, for dilute or weakly absorbing samples, and for use in combined XANES and DRIFTS measurements where we have a reaction cell that can allow for the detection of emitted photons through an X-ray transparent window. Thus, a special reaction cell has been designed by modifying a cell used for combined X-ray and DRIFTS measurements.[25,26]

Cu is a commonly used catalyst for numerous reactions, including CO oxidation ($2CO + O_2 \rightarrow 2CO_2$),[27,28] CO oxidation under H_2-rich steam (CO-PROX),[29,30] methanol synthesis ($CO + H_2 \rightarrow CH_3OH$)[31,32] and the water−gas shift (WGS: $CO + H_2O \rightarrow CO_2 + H_2$).[33,34] The unique ability to convert CO is the key property for supporting Cu over oxides (ZnO, Al_2O_3, CeO_2, TiO_2, etc.) as found typically in industrial processes. Ceria-supported CuO catalysts have attracted attention because of the unique properties of ceria for oxygen storage,[28] ready reducibility, and its ability to firmly anchor Cu, reducing its tendency to sinter. The CuO/CeO_2 catalyst is widely studied and applied for CO oxidation and preferential CO-PROX.[27,29,35] Here, we focus our attention on a catalyst generated by dispersing CuO on CeO_2 nanorods (nr), paying particular attention to the synergistic interactions of its well-constrained reducible oxide support with the supported Cu, and the resulting influence on the catalytic properties. For ceria, three morphologies are most commonly synthesized and studied, including nanorods, nanocubes, and nanospheres.[36] Among the three, ceria nanorods, which mostly expose (100) and (110) faces, were reported as the best catalyst support for CO oxidation.[37]

The CuO/CeO_2 system is a good example of a catalyst where transmission X-ray measurements at the Cu K edge or Ce L_{III} edge are not easy to undertake without diluting the sample in an inert medium (BN or SiO_2). To overcome this obstacle, we designed a novel experiment that combined fluorescence XANES and DRIFTS, and then successfully applied it to an *operando* study of CO oxidation over the new CuO/CeO_2 (nr) catalyst. Our objective was to unravel the role of the different components of the catalyst in the CO oxidation process and to establish if there are specific CuO ↔ CeO_2 interactions that favor the catalysis. With the assistance of *operando* XRD, we have confirmed the exclusive role of surface Cu(I) as the active sites and propose a probable mechanism for the CO oxidation reaction over CuO/CeO_2 catalysts.

2. EXPERIMENTAL SECTION

2.1. The Preparation of 5% CuO/CeO_2 (nr) and CuO Catalysts. Studies reported in the literature for the oxidation of CO on CuO/CeO_2 catalysts show loadings for CuO in the range of 1%−5%. In order to maximize the signals for XANES and DRIFTS, we focus our studies on a 5% CuO/CeO_2 (nr) catalyst. This catalyst was synthesized using wet chemical methods. A procedure available in the literature has been employed to prepare the CeO_2 support in the form of nanorods.[36] For this, $Ce(NO_3)_3{\cdot}6H_2O$ (Aldrich), which was used as the cerium precursor, was dissolved along with NaOH in deionized water. The mixture then was introduced in a Teflon flask of 125 mL filled at 75% of the total volume and, after stirring, was held in a stainless steel autoclave and subjected to hydrothermal treatment during 24 h at 100 °C.

dx.doi.org/10.1021/cs500148e | ACS Catal. 2014, 4, 1650−1661

Scheme 1. Illustration of the Improved Harrick *In Situ* Reaction Cell and the Schematic Explanation for the Instrumental Configuration[a]

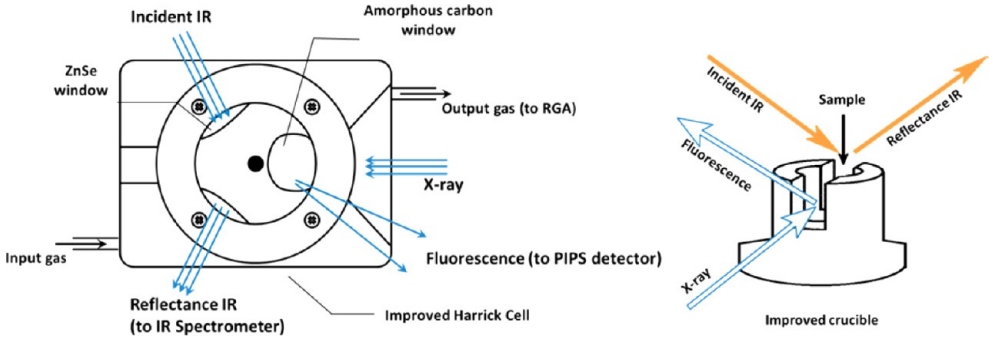

[a]Detailed photographs for the experimental set-up are presented in the Supporting Information.

After the hydrothermal treatment, the precipitates were separated by centrifugation and washed with deionized water and ethanol several times, followed by drying at 60 °C under air overnight. The support then was calcined under air for 2 h at 500 °C. The catalyst of copper supported on the CeO_2 nanorods support (5.0 wt % Cu) was prepared by incipient wetness impregnation with a copper nitrate aqueous solution. Following impregnation, the sample was dried overnight at 100 °C and finally calcined under air at 500 °C for 2 h. The specific surface area for this catalyst (S_{BET}), as determined from analysis of N_2 adsorption isotherms, was 78 m^2 g^{-1}. The commercial CuO nanopowder was obtained from Aldrich (99.99% purity) and is reported to contain particles smaller than 50 nm with a surface area of 29 m^2/g. We did not perform any pretreatment of this sample prior to use.

2.2. TEM and STEM. Sample powder was dispersed as a suspension in deionized water, sonicated for 60 s, deposited dropwise onto a holey carbon grid, and allowed to dry. The high-resolution transmission electron microscopy (TEM) images were collected at 200 kV using a JEOL Model JEM 2100F (Cs ≈ 1 mm) TEM system. The annular dark field (ADF) scanning transmission electron microscopy (STEM) images and electron energy loss spectroscopy (EELS)/energy dispersive X-ray spectroscopy (EDX) spectra were collected with an aberration-corrected Hitachi Model HD-2700C system, which is a dedicated scanning transmission electron microscope operated at 200 kV.

2.3. *Operando* Study Using Combined Fluorescence XANES and DRIFTS and Combined XRD and DRIFTS Methods. The experiments for combined studies with fluorescence XANES and DRIFTS were carried out at beamline 9-BM-C at the Advanced Photon Light Source (APS) at Argonne National Laboratory, in Argonne, IL. Cu K edge (8979 eV) fluorescence XANES spectra were measured from 200 eV below the edge to 300 eV above the edge using a passivated implanted planar silicon (PIPS) detector. XANES spectra were treated employing the Ifeffit package.[38] A Bruker Tensor 37 FTIR spectrometer with side sample compartment was used to collect all infrared (IR) spectra. The gas flow and switching system was composed of a four-channel Brooks flow controller and a Valco switching valve. For the CO/O_2 cycling experiments, the length cycles were 2360 s and the XANES spectra were 380 s. The composition of the outflow gas was analyzed by a residual gas analysis (RGA) device. An improved Harrick Praying Mantis high-temperature reaction cell was used as the *in situ* reaction cell. Inside the cell, double ZnSe windows on the left of the hemisphere dome served as the pathway for the IR beam and the single amorphous carbon window was designed as the path of the emitted fluorescence photons. The schematic of the *in situ* reaction cell as well as the configuration of instruments is illustrated in Scheme 1 (photographs of the beamline setup and the improved cell are shown in the Supporting Information (Figures S1 and S2)). Detailed design of the improved Harrick reaction cell is described elsewhere.[25]

The *operando* study of the CO/O_2 cycling reaction with time-resolved X-ray diffraction (XRD) was carried out at the X7B beamline of the National Synchrotron Light Source (NSLS) at Brookhaven National Laboratory (BNL), which employed a 1.0-mm-OD silica tube *in situ* reaction cell with a thermal resistance heater at its base.[39,40] The XRD patterns were collected by a two-dimensional (2D) Perkin−Elmer image-plate detector. The reaction conditions (i.e., reaction temperature, gas flow rate, and cycling setup) were identical to those used for the experiments conducted at beamline 9-BM-C.

2.4. Procedure of the *Operando* Study. Our *operando* study was composed of four types of experiments. In the first, a commercial CuO powder with an average particle diameter of 50 nm (Aldrich) was heated from room temperature to 250 °C in 2 h under a flow of 20 mL/min 5% CO (balanced by He). The system then was kept at 250 °C for an additional 5 h before cooling. In the second experiment, the 5% CuO/CeO_2 (nr) catalyst was first reduced by 20 mL/min 5% CO (balanced by He) in two successive separate heating stages: from room temperature to 100 °C for 60 min and then maintained at 100 °C for 90 min. After this, it was cooled to room temperature and the cell was heated to 200 °C for 1 h and kept at 200 °C for another 45 min. For the third experiment, the CO oxidation reaction under a constant flow of 18 mL/min of the mixed gases (3.3% CO/1.7% O_2/ 95% He) was studied over a 5% CuO/CeO_2 (nr) catalyst at 100 °C. Finally, in the fourth type of experiment, the CuO/CeO_2 (nr) sample was investigated under CO/O_2 cycles. The gas flow rate was set to 10 mL/min and the ratio of gases in the feed was CO/O_2 = 1. The CO/O_2 cycling experiments were done at 120 °C. The temperature of CO/O_2 cycling and the length of each cycle were optimized with respect to the time resolution of the XANES and DRIFTS measurements. Studies were also carried out using time-resolved XRD.

3. RESULTS AND DISCUSSION

3.1. TEM and STEM Images of the 5% CuO/CeO_2 (nr) Catalyst. The TEM and STEM images of the 5% CuO/CeO_2

dx.doi.org/10.1021/cs500148e | ACS Catal. 2014, 4, 1650−1661

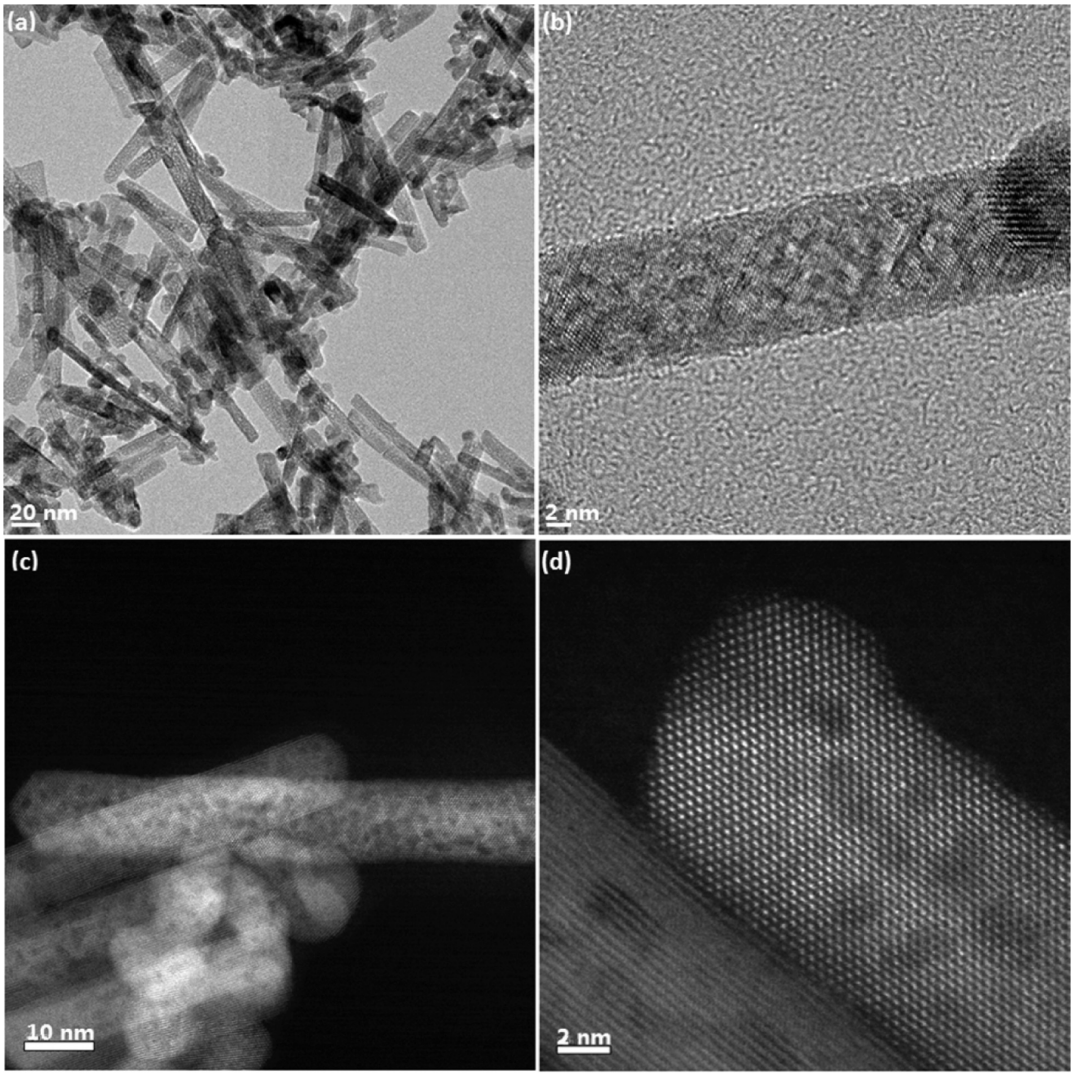

Figure 1. TEM and STEM images of a 5% CuO/CeO_2 (nr) catalyst: (a) TEM, (b) HRTEM, (c) STEM, and (d) HRSTEM.

(nr) catalyst are shown in Figure 1. The TEM image shows that the average diameter of the CeO_2 nanorod supports is ~11 nm in size. Spotlike contrast variations observed in both HRTEM and STEM images are due to voids. In certain nanorods, grain boundaries can also be observed, while a majority of the nanorods were single crystals some were composed of two or more grains. The surface of the ceria nanorods were covered predominately by {100} and {110} facets; in addition, surface steps were also present. No particles of CuO can be discerned from the images, because of the fine dispersion of the Cu species.

3.2. The CO Reduction of CuO Powder. The reduction process of 50-nm-diameter CuO powder by CO was studied by combined fluorescence XANES, DRIFTS, and mass spectrometry (MS) methods in order to unravel the redox properties of isolated bulk CuO without the influence of the CeO_2 substrate. Previous studies have used *in situ* time-resolved XRD or XANES to study the reduction of copper oxides by CO.[41,42] CuO, Cu_4O_3, and Cu_2O are well-known copper oxides with monoclinic, tetragonal, and cubic crystal structures, respectively (see Figure 2). Three possible pathways for the transformation of CuO are shown in Figure 2, including direct reduction (CuO → Cu, pathway 1) and reduction mechanisms, which involve either one intermediate (CuO → Cu_2O → Cu, pathway 2) or

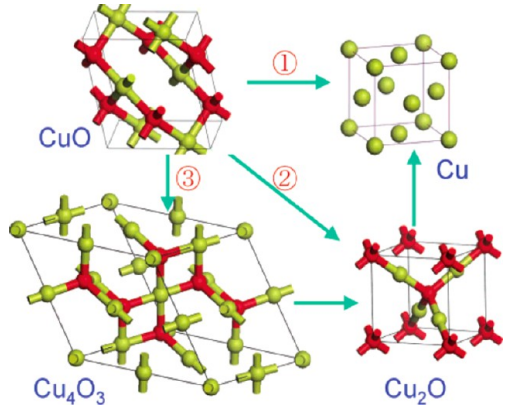

Figure 2. Possible pathways for the reduction of CuO to Cu.

two intermediates (CuO → Cu_4O_3 → Cu_2O → Cu, pathway 3). The *in situ* measurements of XRD and XANES showed a direct transformation pathway for CuO reduction (CuO → Cu) when there was a large supply of CO, while they showed a sequential step pathway involving one intermediate (CuO → Cu_2O → Cu) with a limited supply of CO.[41] Boronin et al. observed the two intermediates pathway (CuO → Cu_4O_3 →

dx.doi.org/10.1021/cs500148e | *ACS Catal.* 2014, 4, 1650−1661

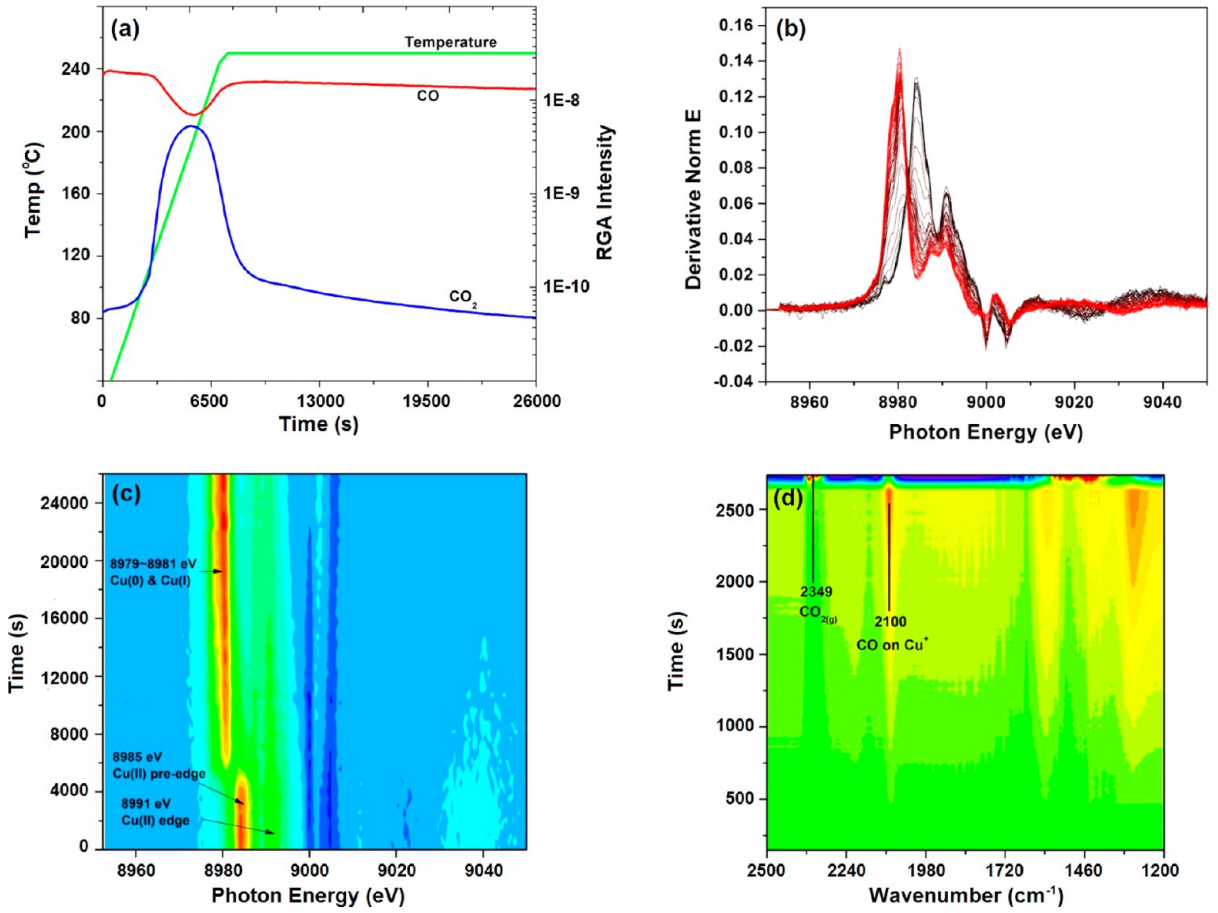

Figure 3. Characterization of a CuO powder under reduction by CO: (a) temperature profile and time-resolved signals for CO and CO_2 in the mass spectrometer, (b) first-derivative XANES spectra, (c) contour map of first-derivative XANES spectra, and (d) contour map of DRIFTS spectra.

$Cu_2O \rightarrow Cu$) over CuO nanopowders in the presence of 10^{-5} mbar of CO.[42] The combination of fluorescence XANES and DRIFTS allows a detailed study of the reaction mechanism and surface species involved in the reduction of copper oxide. Figure 3 summarizes our results. The mass spectral data of CO (m/z = 28) and CO_2 (m/z = 44) (see Figure 3a) showed a single peak for CuO reduction with a temperature range from 80 °C to 250 °C. The MS data also showed a slow decrease of CO_2 when the temperature of the system was kept at 250 °C, which may be ascribed to a slow diffusion controlled reduction of the CuO. First-derivative XANES spectra (see Figures 3b and 3c) were used to monitor the reduction process of CuO.[43] At the beginning of the CO reduction, there were features at 8985 and 8991 eV due to CuO.[43,44] With time, both of the peaks decreased in intensity, which was characteristic of reduction. Definite phase evolution was observed at ∼5000 s after heating, when new features appeared near 8979−8981 eV, which were due to absorption features for Cu(I) and metallic copper, which appear close in energy. At that time, the predominant Cu species was probably changed from CuO or Cu_2O to metallic copper. In correlation with the mass spectrometer signal of CO_2, the partial pressure of CO_2 also reached its maximum. The temperature profile showed that the bulk phase transformation temperature was ∼180 °C. After that temperature, the features of the metallic copper became dominant in the XANES spectra and, by the end of the reduction, no features indicative of oxidized copper could be observed in the XANES data. The $CuO \rightarrow Cu_2O/Cu \rightarrow Cu$ transformation seen in the XANES spectra is in good agreement with the detection of peaks for CuO, Cu_2O, and Cu in time-resolved XRD data for this reduction process.[41] This illustrates the sensitivity of the XANES and diffraction measurements to the composition of the sample.[26,41]

The corresponding DRIFTS spectra are shown in Figure 3d. After 2700 s, only the strong bands of gas-phase CO_2 (2349 cm^{-1}) could be observed and further interpretation of the spectra is not possible because of absorbance saturation of the CO_2 bands. The C−O stretch vibration peak at 2100 cm^{-1}, which arose from the CO adsorption over Cu(I), based on its relatively large thermal stability, characteristic of such species,[27,45] appeared at ∼1000 s and increased in intensity until reliable measurement of spectra stopped at 2700 s. Correlated with the temperature profile, these surface Cu(I) species existed from 60 °C to 85 °C. During this time, the XANES data gave only a weak signal for Cu(I) species (Figure 3c), which became intense only after 4000 s of reduction. Thus, our combined XANES and DRIFTS studies highlight the fact that the spatial composition of the CuO_x sample during reduction in CO may not be uniform, especially near the surface region where DRIFTS has a high sensitivity and can detect the onset of a Cu(II) → Cu(I) at temperatures as low as 60 °C. Eventually, both techniques point to the presence of Cu(I) intermediates in the reduction process.

3.3. The CO Reduction of a CuO/CeO_2 (nr) Catalyst. The CO reduction of the 5% CuO/CeO_2 (nr) catalyst was studied by fluorescence XANES, DRIFTS, and MS. The results

dx.doi.org/10.1021/cs500148e | ACS Catal. 2014, 4, 1650−1661

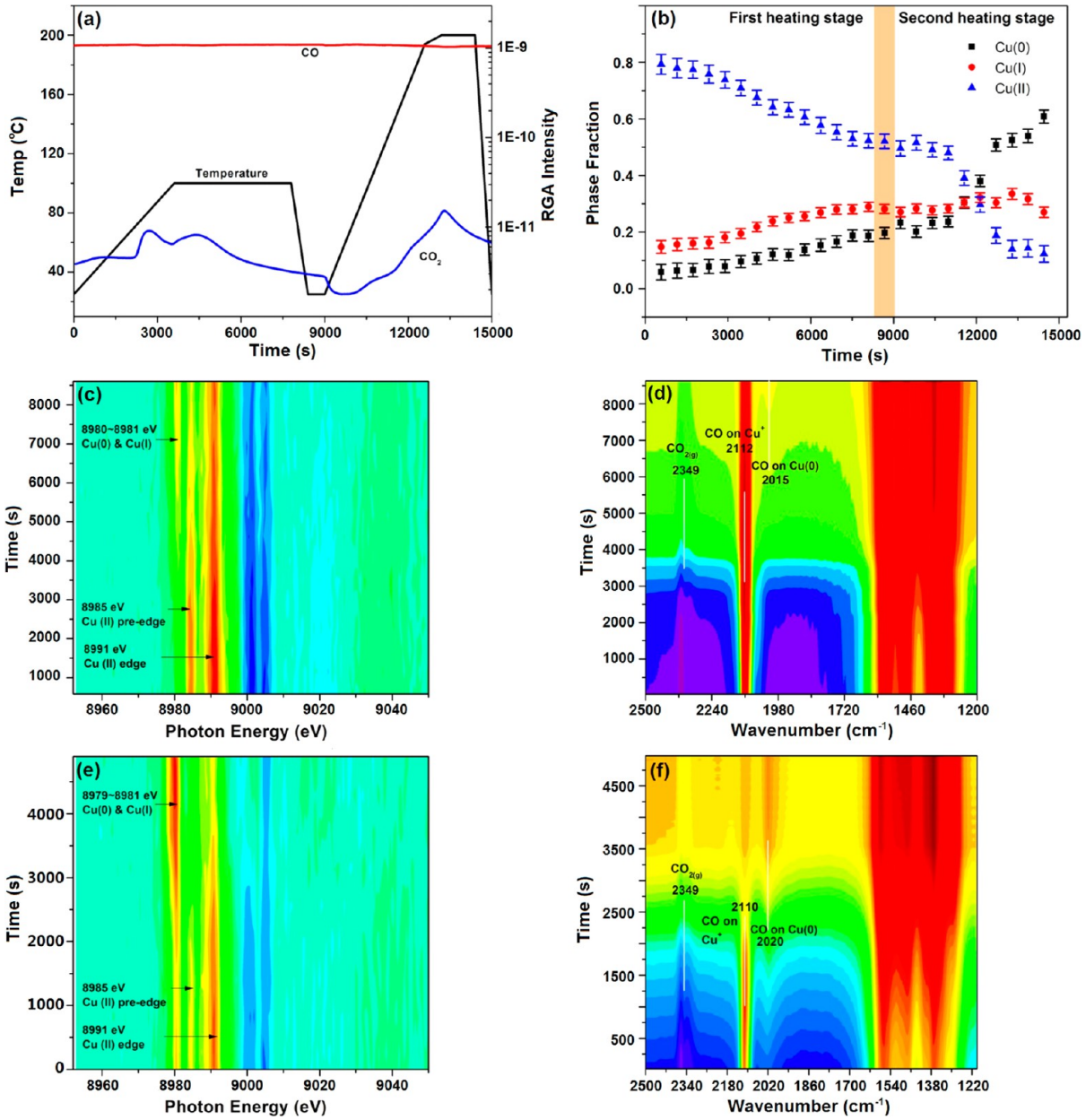

Figure 4. Characterization of a CuO/CeO_2 (nr) catalyst under reduction by CO: (a) the MS signals for CO and CO_2 evolution, along with the heating temperature profile; (b) linear combination fit (LCF) results derived from the XANES data; (c) contour map of the Cu K-edge first-derivative XANES spectra, and (d) DRIFTS spectra during the first heating stage (the corresponding results for the second heating stage are shown in panels (e) and (f)).

from these techniques are summarized in Figure 4. The reduction process was composed of two separate steps. The first step was a ramped heating process in CO from room temperature to 100 °C and the second was a ramping process to 200 °C (the temperature profile is shown in Figure 4a). The first heating process involved moderate temperatures, while the second stage was focused on higher temperatures. The moderate temperatures in the first step of the heating profile were chosen in an attempt to stabilize Cu_4O_3 and Cu_2O intermediates, which could be formed during the reduction of CuO, yielding Cu(I) species.[41] Based on the Cu K-edge first-derivative XANES data shown in Figure 4c, during the first heating stage, the starting Cu species in the catalyst were dispersed Cu(II) oxides with features at 8985 and 8991 eV.[43,44] An additional feature for Cu(I) and Cu(0) appeared near 8980−8982 eV.[43,44] As the temperature was increased, the strength of the two peaks at 8985 and 8991 eV slightly decreased, which indicated a gradual reduction of the CuO species in the catalyst. At 3000 s, after the second heating started in Figure 4e, a strong feature at 8979 eV appeared and increased in intensity with time, which could be regarded as a fingerprint of the bulk phase of metallic copper.[41,43,44] With respect to the temperature profile, the metallic copper appears at ∼87 °C. The evolution of the mixed oxidation states of copper was estimated using a linear combination fit (LCF) method from first-derivative XANES spectra (see Figure 4b). At the end of the first heating stage, the degree of reduction of CuO in the catalyst was ∼40% and we found evidence for the existence of Cu(I) and Cu(0) in XANES. The mass spectrometer signal of CO_2 (m/z = 44) (see Figure 4a) is a

dx.doi.org/10.1021/cs500148e | ACS Catal. 2014, 4, 1650−1661

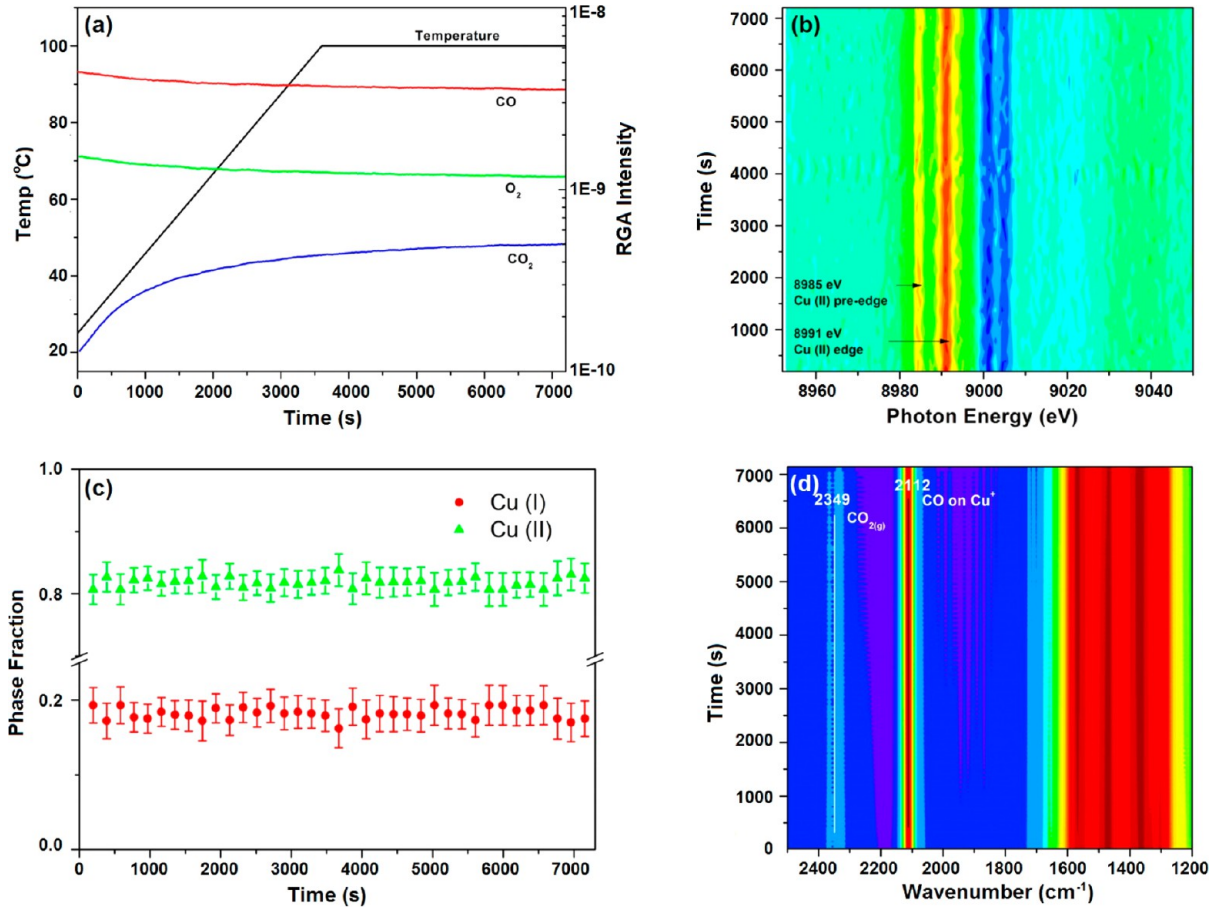

Figure 5. CO oxidation reaction, $2CO + O_2 \rightarrow 2CO_2$, over a CuO/CeO_2 (nr) catalyst: (a) MS signals for CO, O_2, and CO_2 plus temperature profile, (b) contour map of Cu K-edge first-derivative XANES spectra, (c) linear combination fit (LCF) analysis of XANES data, and (d) contour map of DRIFTS spectra. The 5% CuO/CeO_2 (nr) catalyst was under a constant flow of 18 mL/min 3.3% CO/1.7% O_2/He mixed gas, following the temperature profile shown in panel (a) with a final temperature of 100 °C.

strong indication of the reduction of the catalyst with CO, and clearly exhibited two peaks in the first stage. It is likely that, under CO reduction conditions, the CuO/CeO_2 sample is not uniform and the reduction of copper is affected by interactions with the ceria support.[46] The DRIFTS data shown in Figure 4d showed a strong C−O stretch vibration band at 2112 cm^{-1}, which was associated with the adsorbed CO on Cu(I) sites[47] during the heating steps. This phenomenon indicated that Cu(I) was a stable surface species, even at 100 °C under reducing conditions over the CuO/CeO_2 (nr) catalyst. The DRIFTS spectra also showed the formation of bands of 1580, 1430, and 1300 cm^{-1}, which reflected the formation of surface carbonates during the CO reduction on ceria substrates.[48,49] At the end of the first stage (~8000 s), the intensity of the peak at 2112 cm^{-1} slightly decreased (see the three-dimensional (3D) DRIFTS image in the Supporting Information) and a new band at 2015 cm^{-1} appeared, which can be ascribed to CO adsorbed on surface Cu(0), most likely affected by the interaction with the underlying CeO_2 support, as discussed below.[24,34] The appearance of Cu(0) on the surface after 90 min of CO reduction at 100 °C might result from the deep reduction of Cu(I) species, judging from the opposite trend of the two bands. A detailed comparison of the XANES and DRIFTS data in Figures 4c and 4d shows a strong signal in the IR features for Cu(I)−CO when only a weak signal for Cu(I) is seen in XANES. As in the case of CuO reduction, see above, it is likely that the composition of the CuO/CeO_2 (nr) catalyst is not uniform under reduction, with the concentration of Cu(I) being larger near the surface than at the bulk of the sample.

In the second reduction step, the first-derivative XANES spectra exhibited strong increase in intensity at 8979 eV and a loss of intensity at 8985 and 8991 eV at ~140 °C, which indicates that the predominant phase of copper in the catalyst was composed of Cu(0), as shown in Figures 4b and 4c. The DRIFTS data also showed a decrease of surface Cu(I) and an increase of the intensity of the 2020 cm^{-1} band at the same time, indicating that the surface Cu(I) was a minor surface species, yet stable at the temperature range from room temperature to 140 °C over this catalyst under reduction conditions, and would lead to the deeper reduction to metallic copper when the temperature was increased.

The CuO/CeO_2 (nr) catalyst was more easily reduced than the pure CuO powder. Based on the MS data, the reduction of CuO/CeO_2 (nr) started at 70 °C, 10 °C lower than the reduction temperature of the pure CuO powder. Meanwhile, the surface Cu(I) species was more prevalent on the surface of the reduced CuO/CeO_2 (nr) than on the reduced CuO powder. Cu(I) was observed stable by DRIFTS from room temperature to 140 °C on CuO/CeO_2 (nr); in comparison, Cu(I) was only stable in a narrow temperature range, from 60 °C to 85 °C during the reduction of the pure CuO powder.

These phenomena are likely related to the improved copper dispersion as well as the strong copper−ceria interaction. As discussed in previously published articles, there is an interaction

dx.doi.org/10.1021/cs500148e | ACS Catal. 2014, 4, 1650−1661

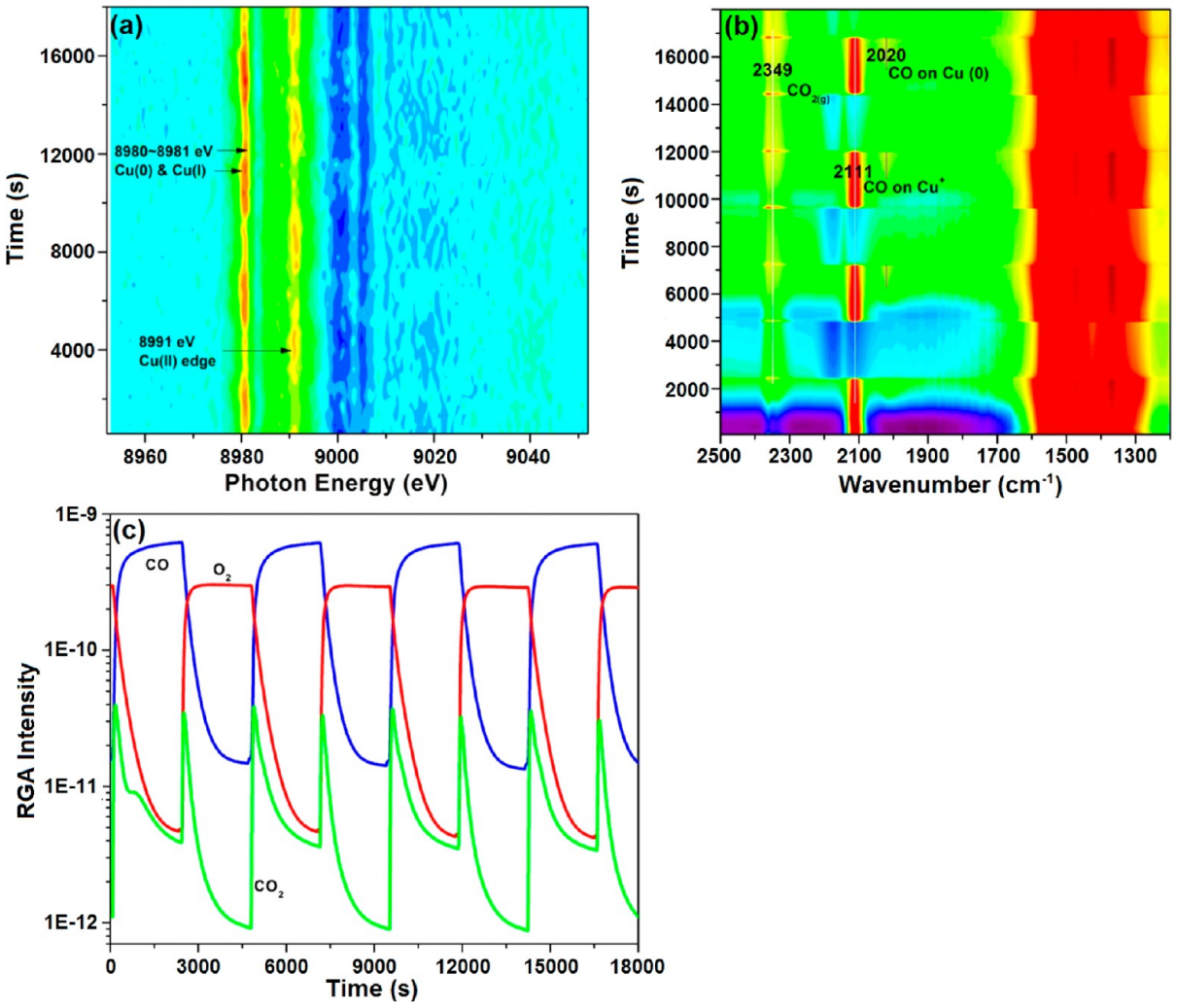

Figure 6. Combined study of XANES, DRIFTS, and MS for CO/O_2 cycling over a 5 wt % CuO/CeO_2 (nr) catalyst: (a) contour map of first-derivative XANES; (b) contour map of DRIFTS; and (c) MS signals for CO, O_2, and CO_2, as a function of time.

at the copper/ceria interface that has a bufferlike effect due to the Ce^{4+}/Ce^{3+} and Cu^{2+}/Cu^{+} redox equilibrium, as shown in eq 3.[50,51]

$$Ce^{4+} + Cu^{+} \leftrightarrow Ce^{3+} + Cu^{2+} \quad (3)$$

This effect makes copper oxide that has been loaded onto a CeO_2 substrate easier to reduce. The equilibrium also decreases the possibility of deep reduction of Cu(I), which expands the Cu(I) stable temperature range. The Cu(0) species observed on the CuO/CeO_2 (nr) catalyst might also be reasonably attributed to copper species at the interface, because, on one hand, it was not observed on CuO powder during reduction and on the other, it performed the opposite trend with Cu(I) at the interface, which resulted from deep reduction of the interfacial Cu(I) species.

3.4. Catalytic CO Oxidation Reaction over a CuO/CeO_2 (nr) Catalyst under the Constant Flow of a CO/O_2 Mixture. The CO oxidation reaction over a 5% CuO/CeO_2 (nr) catalyst was studied under constant flow of a CO and O_2 mixture, at 100 °C. As shown in the MS signal (Figure 5a), the CO conversion increased with heating. At 100 °C, the CO conversion of this system was close to 20%. Time-resolved XANES spectra showed that two strong features at 8985 and 8991 eV, because of Cu(II), remained with the same intensity through the entire reaction (see Figure 5b). Weak features were also detected for Cu(I) in XANES. Using the LCF method, the reduction degree of copper was estimated to be <20% according to XANES (see Figure 5c). The DRIFTS spectra (Figure 5d) exhibited an intense band at 2112 cm^{-1} which indicated that a surface Cu(I) species existed during the entire reaction. No feature for adsorbed CO on Cu(0) could be found. Thus, the result for the catalytic CO oxidation reaction under steady state confirms the relationship between the presence of Cu(I) species and the CO oxidation activity. Notice that, in Figure 5d, strong bands for surface oxo-carbonate species are present from 1600 cm^{-1} to 1200 cm^{-1}.

3.5. CO/O_2 Cycling over a CuO/CeO_2 (nr) Catalyst. Figure 6 shows the results of the combined study of CO/O_2 cycling over a prereduced 5% CuO/CeO_2 (nr) catalyst. The first-derivative XANES spectra show that, during the CO/O_2 cycling, the oxidation state of Cu changed from a partially reduced state in CO to a slightly oxidized state in O_2 atmosphere back and forth with a cyclic intensity change at both 8980−8981 and 8991 eV (i.e., XANES features for Cu(0)/Cu(I) and Cu(II)). Compared with the study of CO reduction of this catalyst, the highest reduced state of Cu was equal to 45% reduction in the CO cycle, while the lowest reduced state was ∼25% reduction in the O_2 cycle. DRIFTS

dx.doi.org/10.1021/cs500148e | ACS Catal. 2014, 4, 1650−1661

spectra (Figure 6b) reveal that during the reduction cycle, the surface of the catalyst was covered by Cu(I) species, which exhibited the C−O stretch vibration band at 2111 cm^{-1}, which was consistent with the steady-state temperature ramp reduction experiment described above for the catalyst. When the gas flow switched to O_2, the surface Cu(I)−CO band vanished and the Cu(I) species was consumed upon oxidation by gas-phase O_2. The band of gas-phase CO_2 at 2349 cm^{-1} only showed a sharp bump during the transition stage of gas switching (i.e., $2CO + O_2 \rightarrow 2CO_2$). A band for adsorbed CO on metallic Cu at 2020 cm^{-1} appeared at the latter part of every CO cycle, which increased in intensity compared with the previous cycle. Meanwhile, the bands at the region of 1600−1200 cm^{-1}, which reflect the surface oxo-carbonate species on ceria, also exhibited a periodic change during CO/O_2 cycling. In the CO-dosing cycle, the absorption of this region increased, indicating the accumulation of carbonate-related species. In the O_2-dosing cycle, the consumption of these species was observed, in agreement with favored decomposition expected for them under oxidizing conditions.[26,27,52] Figure 6c shows the corresponding MS data depicting the consumption of CO and O_2 and the production of CO_2.

The phase fraction estimated from LCF of the first-derivative XANES and the intensity changes of bands for CO on Cu^+ (2111 cm^{-1}), gas-phase CO_2 (2349 cm^{-1}), and CO on Cu(0) (2020 cm^{-1}) in one complete CO/O_2 cycle from 4000 s to 10 000 s were extracted and are displayed in Figure 7. As shown in

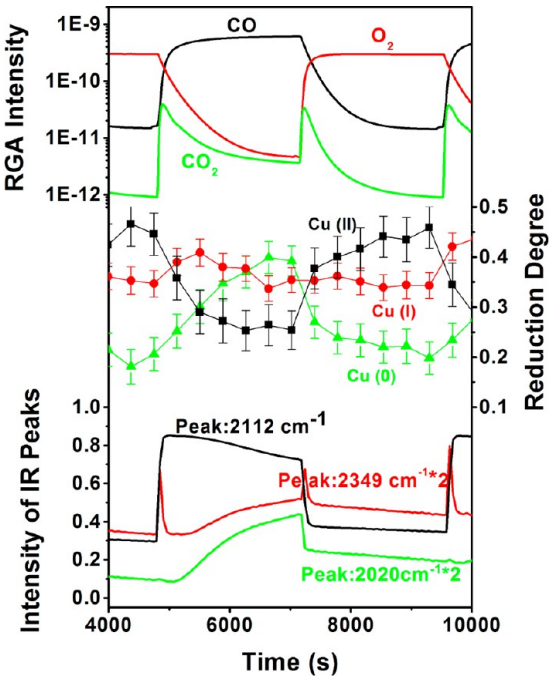

Figure 7. The MS signal (top), the linear-combination-fit result for Cu phase fractions in XANES (middle), and the IR peak-intensity changes for 2020, 2111, and 2349 cm^{-1} features (bottom) in one typical CO/O_2 cycle.

the MS signal, the CO_2 was generated mainly at the time of gas flow switching. The CO_2 decay behaved in a manner similar to the relatively scarce reactant (O_2 in the CO cycle, for example). The minimum partial pressure of CO_2 in the CO cycle was much higher than in the O_2 cycle, which indicated a continuous CO_2 generation during the CO cycle. The LCF result of the Cu K-edge XANES provided an approximate oxidation state change of the predominant phase of Cu, employing the CuO, Cu_2O, and Cu foil as standards. Instant reduction or oxidation was observed when the gas flow was switched, and the catalyst was further reduced or oxidized during the CO or O_2 cycle. The band intensity of CO adsorbed on surface Cu(I) species reached its maximum instantly when the gas flow switched to CO. After that, the band intensity decreased slowly in the CO cycle, even though the partial pressure of CO increased, which indicated that the amount of Cu(I) species decreased in the CO cycle. Meanwhile, the CO adsorbed on metallic copper (2020 cm^{-1}) exhibited an "S"-shaped increase in intensity, which tracked a reverse trend to the band at 2112 cm^{-1}. The intensity change of the gas-phase CO_2 band could be divided into two parts in the reduction cycle. At the time of valve switch, a sharp and narrow bump was observed. After that, the intensity of the 2349 cm^{-1} band dropped to its original level before the switch of the valve and then exhibited an "S"-shaped increase in a manner similar to that of the 2020 cm^{-1} band.

The behavior of the evolution of gas phase CO_2 can be explained as follows. As shown in the mass spectrometer signal, CO and O_2 were both in abundance at the time of gas switching. The sudden increase of gas-phase CO_2 was generated from the catalytic CO oxidation reaction. After that, O_2 in the gas phase was exchanged by CO. Because of the lack of O_2, the yield of CO_2 from the CO oxidation reaction decreased dramatically and, thus, the second increase of CO_2 is probably not a consequence of the catalytic CO oxidation reaction. Instead, it is possible that CO reduced the surface Cu(I) species to metallic copper at this stage. As a result, the second stage of the gas-phase CO_2 increase and the band of CO adsorbed on Cu(0) followed a parallel increasing trend. In other words, catalytic CO oxidation reaction occurred only when the surface Cu(I) species was dominant and metallic copper was scarce, further evidence that the Cu(I) species play a critical role in the redox changes of this reaction. As proved in the steady-state study described above, Cu(I), rather than Cu(0), was the only observed species in the CO oxidation reaction. Therefore, the Cu(I) species over the surface of the catalyst is the most likely and real active phase for the catalytic CO oxidation reaction. This phenomenon also implies that a certain amount of O_2 is essential to stabilize surface Cu(I) and prevent the active sites from deep reduction to metallic copper.

When switched to O_2, the intensity of 2020 cm^{-1} band decreased sharply, accompanied by the quick drop of the 2112 cm^{-1} band when CO could still be detected in a large amount by MS, indicating that both the surface Cu(I) and Cu(0) species were easily oxidized by an excessive amount of O_2, demonstrating that the transformation of both Cu(0) and Cu(I) species to Cu(II) was a fast process. The gas-phase CO_2 band at 2349 cm^{-1} showed sharp peaks at the time of gas switching. At the same time, the band for the adsorption of CO on Cu(0) (2020 cm^{-1}) had decreased to the lowest level, when sufficient reactants and surface Cu(I) existed. This implies that a close relationship exists between surface Cu(I) species and the activity for CO oxidation, while the surface Cu(0) species did not prevail when CO and O_2 were present at the same time. In the O_2 cycle, reoxidation of the copper was confirmed by time-resolved XANES.

To gain a deeper understanding into the mechanism of the CO oxidation reaction, the redox property of ceria supports also needed to be investigated during the CO/O_2 cycling reaction. A time-resolved XRD study was performed to monitor

dx.doi.org/10.1021/cs500148e | ACS Catal. 2014, 4, 1650−1661

the change of the lattice constant of the ceria support, a reported manifestation of the $Ce^{4+} \leftrightarrow Ce^{3+}$ redox property. The nonthermal lattice expansion of ceria is widely accepted as an effective way to observe the formation of oxygen vacancies that result from the reduction of Ce^{4+} to Ce^{3+}.[23,32] The relative phase fraction of crystalline metallic copper, as well as oxidized copper, was also estimated using Rietveld refinement.[53,54] Since the diffraction features of Cu_2O and CuO were broad and weak, it was impossible to separate the relative concentration of these two oxides via XRD, and we refer to them as CuO_x in Figure 8.

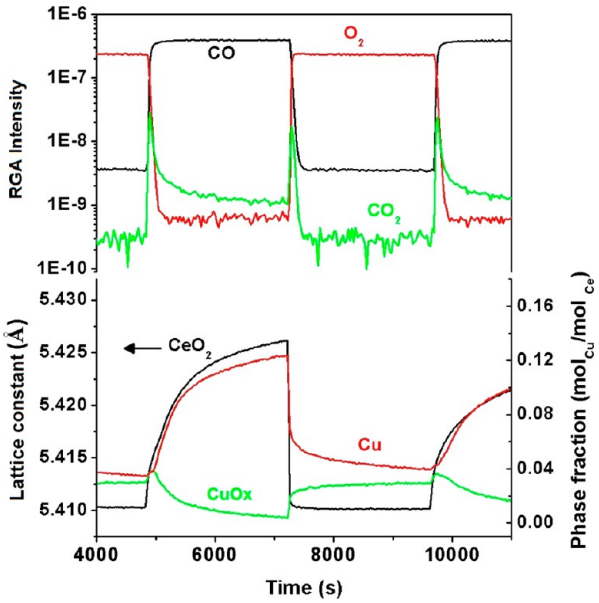

Figure 8. MS signals (top), and the Rietveld-refinement-estimated CeO_2 lattice constant and relative phase fractions of CuO_x and metallic copper (bottom) in one typical CO/O_2 cycle.

All the parameters mentioned above, as well as the MS signals of CO, O_2, and CO_2 in one representative cycle, are shown in Figure 8. The complete CO/O_2 cycling data can be found in the Supporting Information. These figures show that the fresh catalyst is CuO on ceria but oscillates between CuO_x and Cu during subsequent cycles (see Figures S4, S5, and S6 in the Supporting Information). Because of the use of a silica tube flow reactor, the time to reach equilibrium was much shorter than that of the Harrick DRIFTS cell, because of a smaller dead volume. As Figure 8 suggests, instant expansion and contraction were observed when the flow gas switched between CO and O_2, indicating that the reduction and reoxidation of ceria nanorods easily occurred at 120 °C. In the CO cycle, the CeO_2 lattice kept expanding suggesting the continuous reduction of Ce^{4+}. After the O_2 cycle, the lattice constant of ceria dropped to the same level before reduction, which means that the redox conversion of Ce^{4+} is a completely reversible process. The amplitude of ceria expansion decreased with the number of CO/O_2 cycles. This effect might be a consequence of a relaxation, which reduces the strain in the lattice of ceria and makes the creation of oxygen vacancies more difficult. Defects that are initially present in the ceria particles and favor a $Ce^{4+} \rightarrow Ce^{3+}$ reduction are removed during the CO/O_2 cycles. CuO_x and metallic Cu interchangeably formed when the corresponding redox reactant (O_2 or CO) gas was switched. However, the relative phase fraction changes of metallic copper in the CO/O_2 cycles were larger than for CuO_x. Therefore, it is reasonable to conclude that Cu atoms other than those detectable in XRD were involved in the reduction and part of the crystalline metallic copper is likely converted to amorphous or finely dispersed (<3 nm) copper oxides when reoxidized by O_2.

3.6. Mechanism of CO Oxidation Reaction over a CuO/CeO_2 (nr) Catalyst. The mechanism for the catalytic CO oxidation reaction over CuO/CeO_2 has been previously studied by the research groups of Flytzani-Stephanopoulos,[51] Hoçevar,[50] and Martínez-Arias.[27] At low temperature, surface-adsorbed O_2 rather than lattice oxygen is commonly accepted as the source of oxygen.[49] The complete catalytic cycle can be illustrated by four elementary steps, as shown in Scheme 2.

Scheme 2. Proposed Mechanism for the CO Oxidation Reaction over a CuO/CeO_2 Catalyst

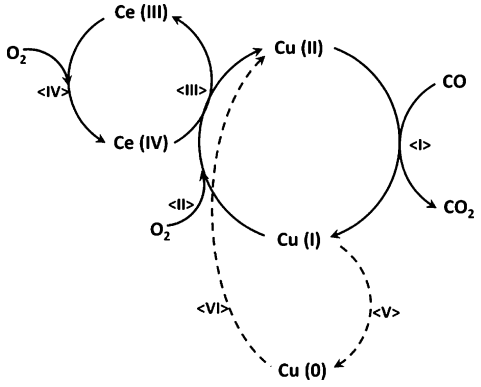

Steps I and II show the reaction mechanism of CO oxidation over bare CuO, in which CO_2 is generated from the CO reduction of Cu(II), thus forming the Cu(I) species, which is oxidized by O_2 to complete the catalytic cycle. Steps III and IV describe the role played by the CeO_2 substrate in the reaction. CeO_2-mediated oxygen transportation reoxidizes the reduced Cu species at the Cu/CeO interface and forms oxygen vacancies that could be filled by adsorbed O_2. The redox relationship of copper and cerium in the catalysts is the key to understanding the reaction mechanism and improving catalytic performance.

$$CO + Cu(II) \rightarrow CO_2 + Cu(I) \quad (I)$$

$$0.5O_2 + Cu(I) - V_0 \rightarrow Cu(II) - O \quad (II)$$

$$Ce^{4+} + Cu(I) \leftrightarrow Ce^{3+} + Cu(II) \quad (III)$$

$$Ce^{3+} - V_0 + 0.5O_2 \rightarrow Ce^{4+} - O \quad (IV)$$

In this work, the cycling study employing a switching valve provided a good opportunity to observe the redox property of copper and ceria supports under non-steady-state conditions, using *operando* characterization methods. A feature for the Cu(0) carbonyl was identified at 2020 cm^{-1} in the DRIFTS spectra. The comparison of CO reduction of CuO powder and CuO/CeO_2 (nr) catalysts, as well as the spectral and stability properties of the adsorbed CO species, indicated that the Cu(0) species is likely located at the Cu/CeO_x interface. The CO/O_2 cycling experiment suggested that the Cu(0) species generated from deeper reduction of the Cu(I) species and was converted back to Cu(II) when switching to O_2. The redox chemistry of Cu(0) species can thus be summarized as steps V and VI, as indicated in Scheme 2 and described below.

dx.doi.org/10.1021/cs500148e | ACS Catal. 2014, 4, 1650−1661

$$CO + Cu(I) \rightarrow CO_2 + Cu(0) \quad (V)$$

$$0.5O_2 + Cu(0) \rightarrow Cu(II) - O \quad (VI)$$

It is commonly accepted that the Cu(0) species are not involved in the catalytic cycle of CO oxidation over copper−ceria catalysts. On one hand, the adsorption of CO on Cu(I) is much stronger than Cu(0); but, on the other hand, the Cu(I) species could be better stabilized at the interface of copper and ceria.[27,50,51] Our CO/O_2 cycling study supports that Cu(0) species do not participate in the catalytic cycle and provides a novel explanation. First, the result of the CO oxidation simulation reaction and CO/O_2 cycling reaction confirmed the coexistence of Cu(I) with the activity of CO oxidation under both steady and nonsteady states. Second, the non-steady-state study also provides information about the relative rate of phase transformation and the stability of different oxidation states of copper. The DRIFTS peak intensity changes for CO on Cu(I) and Cu(0) with gas switching suggest that the reduction from Cu(II) to Cu(I) (step I), as well as the oxidation of Cu(I) and Cu(0) to Cu(II) (steps II and VI) are fast transformation processes. However, the reduction of Cu(I) to Cu(0) (step V) is a slow reaction. As a result, the slow transformation process may not be able to participate in the redox catalytic cycle. Meanwhile, the generation of surface Cu(0) species requires a high concentration of CO alone, which does not exist under CO oxidation conditions.

The results of the *operando* XRD result of CO/O_2 cycling showed that the response of the ceria lattice constant and gas flow switch occurred almost simultaneously. When the gas flow switched to CO, the reduction from Cu(II)/Cu(I) species to Cu(0) was observed starting at the same time of ceria lattice expansion, which implied the interaction of Cu−Ce may enhance the reduction of Cu(II). Therefore, evidence of steps III and IV in the catalytic cycle was established by XRD observation. The reaction rate of steps III and IV is relatively fast, according to the XRD observation. Our study provides a new perspective and evidence which supports the generally accepted CO oxidation mechanism composed of steps I−IV (above). We have shown evidence that these steps, which are involved in the CO oxidation catalytic cycle, are occurring with a fast conversion rate. Steps V and VI are excluded from the probable elementary steps, because of the requirement of the Cu(0) species as well as the relatively slow conversion rate of step V.

4. CONCLUSION

A combination of fluorescence XANES and DRIFTS was used to study the reduction of CuO and CuO/CeO_2 (nr) catalysts by CO. Our combined XANES/DRIFTS studies highlight the fact that the spatial composition of the CuO or CuO/CeO_2 (nr) sample during reduction in CO is not uniform, especially near the surface region where the DRIFTS detects the presence of a significant concentration of Cu(I) species not seen with XANES during the early stages of the reduction process. The CuO/CeO_2(nr) catalyst was dynamic in its behavior with the relative ratios of Cu(II)/Cu(I)/Cu(0) changing as a function of temperature and reactant pressure during the catalytic process. A comparison of the reduction of CuO powder and CuO/CeO_2 (nr) proved the effect of strong metal ↔ support interaction between copper and ceria in the catalyst.

Operando fluorescence XANES/DRIFTS, as well as *operando* XRD techniques, were important to investigate the CO oxidation reaction on the CuO/CeO_2 (nr) catalyst. CO/O_2 cycling experiments employing a quick switching valve system showed the dynamic nature of the catalyst components and provided convincing evidence that the surface-dispersed Cu(I) species rather than Cu(0) are the active species for the CO oxidation reaction. Kinetic evidence was also provided to support that the Cu^{2+}/Cu^{+} and Ce^{4+}/Ce^{3+} species were involved in the redox mechanism of CO oxidation over the Cu/CeO_x catalysts.

Furthermore, with the design of a new reaction cell, which introduces fluorescence XANES into combined *operando* studies with DRIFTS and mass spectrometry, we successfully expanded the application range of *in situ* characterization techniques. Although the time resolution remains to be improved, this combination of techniques in one experiment shows great potential for mechanistic studies of catalysts containing high-*Z* atoms as part of their active phase.

■ ASSOCIATED CONTENT

Supporting Information

XRD pattern of CuO/CeO_2 (nr) catalyst (Figure S1), instrument setup and photos of reaction cell (Figures S2 and S3), three-dimensional (3D) figure of DRIFTS of CuO reduction (Figure S4), and Rietveld refinement result of time-resolved XRD measurement (Figures S5 and S6). This material is available free of charge via the Internet at http://pubs.acs.org.

■ AUTHOR INFORMATION

Corresponding Author

*E-mail: ssenanay@bnl.gov.

Notes

The authors declare no competing financial interest.

■ ACKNOWLEDGMENTS

The research carried out at the Chemistry Department, the National Synchrotron Light Source (NSLS), and the Center for Functional Nanomaterials (CFN), at Brookhaven National Laboratory (BNL) was supported by the Division of Chemical Sciences, Geosciences, and Biosciences, Office of Basic Energy Sciences of the U.S. Department of Energy (Contract No. DE-AC02-98CH10886). Use of the Advanced Photon Source, an Office of Science User Facility operated for the U.S. Department of Energy (DOE) Office of Science by Argonne National Laboratory, was supported by the U.S. DOE under Contract No. DE-AC02-06CH11357. The financial support from China Scholarship Council (File No. 201206010107) is gratefully acknowledged. Financial support from MINECO (Plan Nacional Project No. CTQ2012-32928) and EU COST CM1104 action is also acknowledged. Thanks are also due to ICP-CSIC Unidad de Apoyo for S_{BET} measurement.

■ REFERENCES

(1) Steele, B. C. H.; Heinzel, A. *Nature* **2001**, *414* (6861), 345−352.
(2) Huber, G. W.; Iborra, S.; Corma, A. *Chem. Rev.* **2006**, *106* (9), 4044−4098.
(3) Marchetti, J. M.; Miguel, V. U.; Errazu, A. F. *Renewable Sustainable Energy Rev.* **2007**, *11* (6), 1300−1311.
(4) Hoffmann, M. R.; Martin, S. T.; Choi, W. Y.; Bahnemann, D. W. *Chem. Rev.* **1995**, *95* (1), 69−96.
(5) Herein, D. *Handb. Heterog. Catal.* **2008**, *3*, 765−774.
(6) Singh, J.; Lamberti, C.; van Bokhoven, J. A. *Chem. Soc. Rev.* **2010**, *39* (12), 4754−4766.

(7) Weckhuysen, B. M. *Angew. Chem., Int. Ed.* **2009**, *48* (27), 4910−4943.
(8) Bentrup, U. *Chem. Soc. Rev.* **2010**, *39* (12), 4718−4730.
(9) Frenkel, A. I.; Rodriguez, J. A.; Chen, J. G. *ACS Catal.* **2012**, *2* (11), 2269−2280.
(10) Becker, E.; Carlsson, P.-A.; Kylhammar, L.; Newton, M. A.; Skoglundh, M. *J. Phys. Chem. C* **2011**, *115* (4), 944−951.
(11) Ferri, D.; Newton, M. A.; Nachtegaal, M. *Top. Catal.* **2011**, *54* (16−18), 1070−1078.
(12) Kubacka, A.; Martinez-Arias, A.; Fernandez-Garcia, M.; Newton, M. A. *Catal. Today* **2009**, *145* (3−4), 288−293.
(13) Marcelli, A.; Innocenzi, P.; Malfatti, L.; Newton, M. A.; Rau, J. V.; Ritter, E.; Schade, U.; Xu, W. *J. Synchrotron Rad.* **2012**, *19*, 892−904.
(14) Newton, M. A. *Top. Catal.* **2009**, *52* (10), 1410−1424.
(15) Newton, M. A.; Dent, A. J.; Fiddy, S. G.; Jyoti, B.; Evans, J. *Catal. Today* **2007**, *126* (1−2), 64−72.
(16) Newton, M. A.; Dent, A. J.; Fiddy, S. G.; Jyoti, B.; Evans, J. *Phys. Chem. Chem. Phys.* **2007**, *9* (2), 246−249.
(17) Newton, M. A.; Di Michiel, M.; Kubacka, A.; Iglesias-Juez, A.; Fernandez-Garcia, M. *Angew. Chem., Int. Ed.* **2012**, *51* (10), 2363−2367.
(18) Newton, M. A.; Jyoti, B.; Dent, A. J.; Fiddy, S. G.; Evans, J. *Chem. Commun.* **2004**, No. 21, 2382−2383.
(19) Newton, M. A.; Di Michiel, M.; Kubacka, A.; Fernández-García, M. *J. Am. Chem. Soc.* **2010**, *132* (13), 4540−4541.
(20) Marinkovic, N. S.; Wang, Q.; Barrio, L.; Ehrlich, S. N.; Khalid, S.; Cooper, C.; Frenkel, A. I. *Nucl. Instrum. Methods Phys. Res., Sect. A* **2011**, *649* (1), 204−206.
(21) Marinkovic, N. S.; Wang, Q.; Frenkel, A. I. *J. Synchrotron Rad.* **2011**, *18*, 447−455.
(22) Pascarelli, S.; Mathon, O. *Phys. Chem. Chem. Phys.* **2010**, *12* (21), 5535−5546.
(23) Newville, M. *Fundamentals of XAFS*; Consortium for Advanced Radiation Sources, University of Chicago, Chicago, IL, 2004.
(24) Barrio, L.; Estrella, M.; Zhou, G.; Wen, W.; Hanson, J. C.; Hungría, A. B.; Hornés, A.; Fernández-García, M.; Martínez-Arias, A.; Rodriguez, J. A. *J. Phys. Chem. C* **2010**, *114* (8), 3580−3587.
(25) Beyer, K. A.; Zhao, H.; Borkiewicz, O. J.; Newton, M. A.; Chupas, P. J.; Chapman, K. W. *J. Appl. Crystallogr.* **2014**, *47*, 95−101.
(26) Hanson, J. C.; Si, R.; Xu, W.; Senanayake, S. D.; Mudiyanselage, K.; Stacchiola, D.; Rodriguez, J. A.; Zhao, H.; Beyer, K. A.; Jennings, G.; Chapman, K. W.; Chupas, P. J.; Martínez-Arias, A. *Catal. Today* **2014**, *229* (0), 64−71.
(27) Martinez-Arias, A.; Fernandez-Garcia, M.; Soria, J.; Conesa, J. C. *J. Catal.* **1999**, *182* (2), 367−377.
(28) Trovarelli, A. *Catal. Rev.−Sci. Eng.* **1996**, *38* (4), 439−520.
(29) Gamarra, D.; Lopez Camara, A.; Monte, M.; Rasmussen, S. B.; Chinchilla, L. E.; Hungria, A. B.; Munuera, G.; Gyorffy, N.; Schay, Z.; Cortes Corberan, V.; Conesa, J. C.; Martinez-Arias, A. *Appl. Catal., B* **2013**, *130*, 224−238.
(30) Marino, F.; Descorme, C.; Duprez, D. *Appl. Catal., B* **2005**, *58* (3−4), 175−183.
(31) Chinchen, G. C.; Waugh, K. C.; Whan, D. A. *Appl. Catal.* **1986**, *25* (1−2), 101−107.
(32) Liu, X. M.; Lu, G. Q.; Yan, Z. F.; Beltramini, J. *Ind. Eng. Chem. Res.* **2003**, *42* (25), 6518−6530.
(33) Wang, X. Q.; Rodriguez, J. A.; Hanson, J. C.; Gamarra, D.; Martinez-Arias, A.; Fernandez-Garcia, M. *J. Phys. Chem. B* **2006**, *110* (1), 428−434.
(34) Gokhale, A. A.; Dumesic, J. A.; Mavrikakis, M. *J. Am. Chem. Soc.* **2008**, *130* (4), 1402−1414.
(35) Huber, H.; Kundig, E. P.; Moskovits, M.; Ozin, G. A. *J. Am. Chem. Soc.* **1975**, *97* (8), 2097−2106.
(36) Mai, H.-X.; Sun, L.-D.; Zhang, Y.-W.; Si, R.; Feng, W.; Zhang, H.-P.; Liu, H.-C.; Yan, C.-H. *J. Phys. Chem. B* **2005**, *109* (51), 24380−24385.
(37) Tana; Zhang, M.; Li, J.; Li, H.; Li, Y.; Shen, W. *Catal. Today* **2009**, *148* (1−2), 179−183.
(38) Ravel, B.; Newville, M. *J. Synchrotron Rad.* **2005**, *12*, 537−541.
(39) Xu, W.; Si, R.; Senanayake, S. D.; Llorca, J.; Idriss, H.; Stacchiola, D.; Hanson, J. C.; Rodriguez, J. A. *J. Catal.* **2012**, *291*, 117−126.
(40) Chupas, P. J.; Chapman, K. W.; Kurtz, C.; Hanson, J. C.; Lee, P. L.; Grey, C. P. *J. Appl. Crystallogr.* **2008**, *41*, 822−824.
(41) Wang, X. Q.; Hanson, J. C.; Frenkel, A. I.; Kim, J. Y.; Rodriguez, J. A. *J. Phys. Chem. B* **2004**, *108* (36), 13667−13673.
(42) Svintsitskiy, D. A.; Kardash, T. Y.; Stonkus, O. A.; Slavinskaya, E. M.; Stadnichenko, A. I.; Koscheev, S. V.; Chupakhin, A. P.; Boronin, A. I. *J. Phys. Chem. C* **2013**, *117* (28), 14588−14599.
(43) Lamberti, C.; Bordiga, S.; Bonino, F.; Prestipino, C.; Berlier, G.; Capello, L.; D'Acapito, F.; Xamena, F.; Zecchina, A. *Phys. Chem. Chem. Phys.* **2003**, *5* (20), 4502−4509.
(44) Sipr, O.; Simunek, A.; Bocharov, S.; Kirchner, T.; Drager, G. *J. Synchrotron Rad.* **2001**, *8*, 235−237.
(45) Gamarra, D.; Belver, C.; Fernández-García, M.; Martínez-Arias, A. *J. Am. Chem. Soc.* **2007**, *129* (40), 12064−12065.
(46) Zheng, X. C.; Zhang, X. L.; Wang, X. Y.; Wang, S. R.; Wu, S. H. *Appl. Catal., A* **2005**, *295* (2), 142−149.
(47) Bera, P.; Lopez Camara, A.; Hornes, A.; Martinez-Arias, A. *J. Phys. Chem. C* **2009**, *113* (24), 10689−10695.
(48) Vayssilov, G. N.; Mihaylov, M.; St Petkov, P.; Hadjiivanov, K. I.; Neyman, K. M. *J. Phys. Chem. C* **2011**, *115* (47), 23435−23454.
(49) Pozdnyakova, O.; Teschner, D.; Wootsch, A.; Krohnert, J.; Steinhauer, B.; Sauer, H.; Toth, L.; Jentoft, F. C.; Knop-Gericke, A.; Paal, Z.; Schlogl, R. *J. Catal.* **2006**, *237* (1), 1−16.
(50) Sedmak, G.; Hocevar, S.; Levec, J. *J. Catal.* **2003**, *213* (2), 135−150.
(51) Liu, W.; Flytzani-Stephanopoulos, M. *J. Catal.* **1995**, *153* (2), 304−316.
(52) Camara, A. L.; Monte, M.; Martinez-Arias, A.; Conesa, J. C. *Catal. Sci. Technol.* **2012**, *2* (12), 2436−2439.
(53) Larson, A. C.; D, R. B. V. *Technical Report LAUR 86-748*, Los Alamos National Laboratory, Albuquerque, NM, 2000.
(54) Toby, B. H. *J. Appl. Crystallogr.* **2001**, *34*, 210−213.